Magnetically induced femtoscale strain modulations in $HoMn_2O_5$

C. Vecchini,[1,2] A. Bombardi,[1] L. C. Chapon,[3,4] G. Beutier,[5] P. G. Radaelli,[6] S. Park,[7] and S.-W. Cheong[7]

[1]*Diamond Light Source Ltd, Harwell Science and Innovation Campus, Didcot, Oxfordshire, OX11 0DE, United Kingdom*

[2]*National Physical Laboratory, Hampton Road, Teddington, TW11 0LW, United Kingdom*

[3]*ISIS Facility, Rutherford Appleton Laboratory - STFC, OX11 0QX, Chilton, Didcot United Kingdom*

[4]*Institut Laue-Langevin, BP 156X, 38042, Grenoble, France*

[5]*SIMaP, UMR 5266 CNRS Grenoble-INP UJF, BP 75, 38402 Saint Martin dHères, France*

[6]*Department of Physics, University of Oxford, Parks Road, Oxford OX1 3PU, United Kingdom*

[7]*Rutgers Center for Emergent Materials and Department of Physics & Astronomy, Rutgers University, Piscataway, New Jersey 08854, USA*

(Received 29 October 2013; revised manuscript received 17 February 2014; published 17 March 2014)

X-ray scattering was used to investigate the magnetically induced ionic displacements in the low-temperature commensurate ferroelectric/antiferromagnetic phase of the multiferroic $HoMn_2O_5$. The structural modulation signal appearing at twice the magnetic wave vector $\mathbf{k}_m = (\frac{1}{2}\ 0\ \frac{1}{4})$ has been used, combined with symmetry analysis, to determine a model for the ionic displacements up to a precision of 10^{-3} Å. The symmetry-breaking operations that are associated to the active irreducible representation have been experimentally determined from the analysis of the modulation modes. They reveal a lowering of symmetry to the polar point group $m2m$. Calculations based on the determined model show that the magnetic structure along the c direction is stabilized via nearest-neighbor and next-nearest-neighbor interactions through the rare-earth layer. We also show that by knowing both the magnetic and the magnetically induced strain waves patterns, it is possible to remove any phase ambiguity between the crystal and magnetic structures.

DOI: 10.1103/PhysRevB.89.125114 PACS number(s): 75.50.Ee, 75.30.Gw, 75.85.+t, 78.70.Ck

I. INTRODUCTION

In all magnetic systems, the onset of magnetic order leads to magnetostriction effects, which can also induce the onset of charge modulation in materials [1]. Density waves in the charge distribution could be due either to a periodically distorted lattice, with each ion retaining its equilibrium charge, often referred as strain wave, or by a periodic excess and deficit of charge on the sites of an undistorted lattice (charge density wave). Strain waves have been studied since the 1970s, for example in chromium [2–4], and can provide a very convenient tool for the study of magnetic domain populations [5] as well as magnetic propagation vectors [6] or multi-**k** structures [7]. In magnetoelectric multiferroic materials [8], where magnetism and ferroelectricity coexist and couple, the study of strain waves and their relation with the magnetic structure can be of particular interest for the fundamental understanding of ordering phenomena. The system presented in this study belongs to the RMn_2O_5 family (R = rare-earth or Y, Bi), whose members have a complex orthorhombic crystal structure (space group *Pbam*). At low temperature, they exhibit a rich magnetic phase diagram due to a complex pattern of magnetic interactions. Upon cooling, at $T_{N1} \sim 40$ K, $HoMn_2O_5$ becomes antiferromagnetic with an incommensurate (ICM) magnetic order, which locks into a commensurate (CM) structure at $T_N \sim 36$ K, characterized by anomalies in the dielectric constant and the presence of spontaneous electric polarization. A further phase transition to a reentrant incommensurate phase appears at $T_{\text{LT-ICM}} \sim 18$ K, which is accompanied with an abrupt decrease of spontaneous polarization. Symmetric magnetic exchange has been recognized to be the primary origin of the spontaneous electric polarization (**P**) observed in the commensurate magnetic phases of RMn_2O_5 systems [9–11], although a smaller antisymmetric exchange contribution has also been observed (R = Y, Ho, Tb) [12]. In this family of compounds, polar displacements due to the structural relaxation induced by competing Heisenberg terms ($\mathbf{J}_{ij}\mathbf{S}_i \cdot \mathbf{S}_j$) and by Dzyaloshinskii-Moriya terms ($\mathbf{D_{ij}} \cdot \mathbf{S_i} \times \mathbf{S_j}$) in the magnetic Hamiltonian lead to small **P** values compared to proper ferroelectrics. The ionic displacements due to magnetostriction are predicted to be of the order 10^{-4} Å in magnitude [13] and as such are not measurable by laboratory crystallography instruments. A recent experiment to determine the induced lattice distortions in the perovskite multiferroic $TbMnO_3$ has been successfully performed by Walker *et al.* [14] by using a combination of electric and magnetic fields (>2 T) to produce a single magnetic domain state and to switch on the linear magnetoelastic coupling [15]. In these conditions, an interference between charge and magnetic x-ray scattering arose, which encoded the amplitude and phase of the displacements. When combined with a theoretical analysis, the data measured at the first harmonic $\mathbf{k_m}$ ($\mathbf{k_m}$ representing the magnetic propagation vector), which correspond to the biquadratic coupling term in the free energy expansion $(\mathbf{k_m} \cdot \mathbf{k_c})^2$, where $\mathbf{k_c}$ represents the lattice modulation, allowed Walker's team to resolve the ionic displacements at the femtoscale. Nowadays it is possible to determine femtoscale distortions occurring at $2\mathbf{k_m}$ originating from the third-order linear-quadratic term $\mathbf{k_m^2} \cdot \mathbf{k_c}$, using synchrotron radiation and large area photon counting detectors. This approach can be applied to all magnetic systems showing magnetostriction effects or to materials where secondary order parameters lead to subtle lattice distortions. The magnetostrictive interactions, and therefore the corresponding displacements, are invariant in a general reversal of the moments, and for a magnetic structure with propagation vector $\mathbf{k}_m$, the period of the charge modulation is half the period of the magnetic modulation [16,17]. In the RMn_2O_5 case, it has been shown that the $\mathbf{k}_c$ ($\mathbf{k}_c = 2\mathbf{k}_m$) modulation is induced by the main (magnetic) order parameter. In a previous experiment [18] the temperature

dependence of the (4 4 0.5) satellite reflection was measured and the quadratic law dependence with respect to a magnetic (2.5 3 0.25) reflection agrees with the time-reversal symmetry invariance requiring the lattice distortion $L \propto M^2$ at the leading term. Therefore the structural displacements induced by the magnetic structure can be investigated by the modeling of such satellite charge reflections. Here a systematic measurement of those superlattice reflections was performed. A displacement model to determine the modulation pattern arising from the frustration of the underling magnetic structure was found. The magnetic transition breaks the inversion symmetry and in the CM phase the system goes into a polar group. Several experiments support a lowering of symmetry at least to the space group $Pb2_1m$, however as the distortions are tiny, no direct evidence of a symmetry-breaking transition could be obtained from x-ray diffraction till now [19,20].

II. EXPERIMENTAL

A high-quality single crystal ($1 \times 1 \times 3$ mm^3) of $HoMn_2O_5$ grown using flux method [12] was used for the x-ray scattering experiment, performed at the I16 beamline (Diamond Light Source Ltd., UK) [21,22]. The sample was mounted on the beamline κ diffractometer in a closed cycle refrigerator (CCR) with base temperature of ~5 K. The crystal was oriented with the diffraction face perpendicular to the (110) direction. The diffractometer was operated in the vertical plane scattering mode with linear horizontal polarization of the incident beam and the photon energy was tuned to 14 keV. This energy was chosen in order to maximize the scattering volume and the access to reciprocal space while still maintaining a good detector efficiency of about 60% (320 μm thick Si sensors). Two Rh coated mirrors were used to focus the beam to 30×180 μm^2 and high harmonic contaminations suppression. A Dectris® Pilatus 100K single-photon-counting area detector has been used throughout the whole experiment. This detector combines high resolution with extremely small point spread and a large dynamic range (20 bits), essential requirements to be able to collect weak superlattice reflections as well as the strong Bragg charge reflections. At this energy, harmonic contaminations can be omitted in the calculations: the mirrors transmission for the second harmonic ($E = 28$ keV) is <1% whereas the detector efficiency decreases to ~10%. Moreover the flux provided by the undulator will be much decreased due to its optimization for 14 keV and of the peak intensity of the flux provided by the synchrotron itself, which leads to a further decrease of intensities of more than one order of magnitude. Finally the ratio of the monochromator structure factor for the Si333 and the Si111 is about half, while for the Si222 is vanishingly small. We measured the integrated intensities of 455 reflections at position $(h,k,l + 1/2)$ in the commensurate (CM) magnetic phase at $T = 22$ K. A dataset in the paramagnetic phase at $T = 45$ K was also collected using the same statistics for background subtraction. Due to the CCR vibrations together with the sphere of confusion of the κ diffractometer (~80 μm^3) and the possible nonhomogeneity of the sample surface, it is possible to switch between different grains or even probe several grains at the same time, making the data analysis extremely challenging. Therefore most care was given to probe the sample surface by collecting 85 reflections in a different position on the sample surface, again both in the CM and in the paramagnetic phases, to be used as a consistency check. Moreover we measured several charge reflections with the purpose to determine the scaling factor for quantitative analysis. The data were then corrected for background and possible harmonic contaminations by pixel-by-pixel subtraction of the high-temperature data and then corrected for geometrical (self-)absorption and Lorentz factor, multiplying them by the factor $A(\mathbf{Q},\psi) \cdot L(\mathbf{Q}) = [1 + \frac{\sin\alpha(\mathbf{Q},\psi)}{\sin\beta(\mathbf{Q},\psi)}] \cdot \sin 2\theta(\mathbf{Q})$ where $\alpha(\mathbf{Q},\psi)$ and $\beta(\mathbf{Q},\psi)$ are the incident and exit angles with respect to the crystal surface, with no need for polarization correction in this geometry. The intensities were all treated as not equivalent, regardless of symmetry operations. The corrected integrated intensities were then used to analyze the distortion pattern with the FULLPROF program suite [23], by using the propagation vector formalism, in which the displacements for all sites are expanded in Fourier series. For the superstructure with propagation vector $\mathbf{k}_c$, the displacement $\mathbf{u}_n$ of an atom in the nth cell is calculated as:

$$\mathbf{u}_n = \mathbf{D}_n(-1)^n. \quad (1)$$

The components of the vectors $\mathbf{D}$ are defined in term of Cartesian components D_x, D_y, D_z for each n, which are sufficient to fully determine the superstructure. Constraints exists between $\mathbf{D}_n$ for symmetry-related sites, these constraints are determined by representation analysis and will be described below.

III. RESULTS AND DISCUSSION

Superlattice reflections are typically weaker than the fundamental ones by a a factor larger than 10^6. The rocking curve of a fundamental charge (8 8 2) and a very strong superlattice (SL) (7 9 0.5) reflections are shown in Fig. 1. The FWHM for a rocking curve on a typical superlattice reflection on $HoMn_2O_5$ is σ ~0.03° (in θ), value that is comparable to the FWHM observed for the fundamental ones, hence the ionic displacements show long-range order. The temperature dependence of two superlattice reflections (7,9,0.5) and (6,7,−0.5) have been collected in the temperature range $5\text{ K} < T < 45$ K and is shown in Fig. 2. The appearance of the $\mathbf{k}_c$ reflections coincides with the onset of the long-range magnetic order ($T_{N1} \sim 40$ K), which develops in a CM magnetic structure at ~36 K where an abrupt change of slope is observed. Further cooling in this

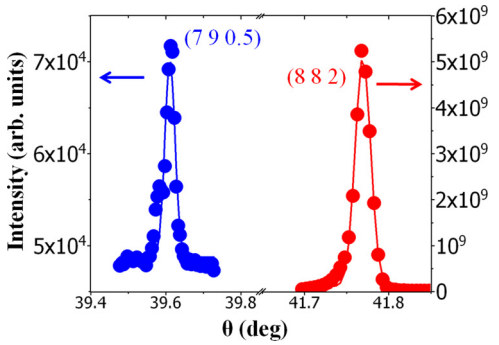

FIG. 1. (Color online) Peak profiles of the (7 9 0.5) and (8 8 2). The line is a fit to the data with a Lorentian profile function.

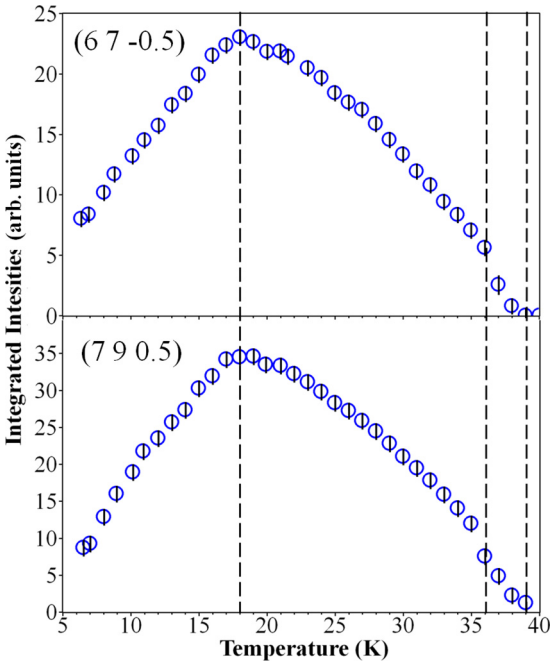

FIG. 2. (Color online) Temperature dependence of integrated intensities of SL peaks: (6 7 −0.5) (top panel) and (7 9 0.5) (bottom panel).

phase leads to the observation of maximum intensities at about 18 K for both measured reflections, followed by a decrease due to the low-temperature CM to ICM magnetic phase transition. These features are in very good agreement with previously reported neutron and magnetization measurements [24]. The change in the signal observed in the low-temperature phase ($T < T_{\text{LT-ICM}} \sim$) is also in agreement with the expectation of a modified ionic displacements pattern due to the change in the magnetic structure. At 14 keV, the separation between, e.g., (4.96 8 0.56) and (4.96 8 0.44) is $\leqslant \sigma$. This doesn't allow a complete deconvolution of the four split ICM peak positions [although the separation between (0.96 0 0.56) and (1.04 0 0.44) is large, $>5\sigma$ and can be separated]. The change in intensity in this phase is smoother than the previously reported one for the $TbMn_2O_5$ case [25] but in good agreement with the previously reported data on $HoMn_2O_5$[18].

An initial attempt to use an unconstrained model to fit the data has been performed but due to the large number of free parameters, a stable fit could not be achieved: the completely unconstrained model involves up to 97 free parameters: 32 atoms per unit cell with x,y,z displacements components and a global scale factor. The latter has been determined with the use of few charge reflections in the refinements, which have been corrected for self-absorption. In order to reduce the number of free parameters during data modeling, we used the symmetry mode analysis method. The symmetry properties of a distortion mode are characterized by an irreducible representation (Irrep) of the high-symmetry space group, defining the mode transformation properties under the operations of this group. Therefore we first determined a basis of symmetry modes of the parent phase (*Pbam* space group) compatible with the low symmetry phase, and then we decomposed the structural distortion as a sum of the contributions of all of them. We used the computer program BASIREPS, part of the FULLPROF suite, to perform the symmetry analysis [23] and the programs ISOTROPY [26] and AMPLIMODES [27], the latter from the Bilbao Crystallographic Server [28–30].

As shown in Table I, there are eight one-dimensional Irreps allowed for the *Pbam* space group for the wave vector $\mathbf{k}_c = (0\ 0\ 0.5)$. For each Irrep, the number of free parameters varies between 12 and 14. An initial least-square refinement for each of the eight Irreps lead to very poor agreement factors. The best fits (with a single Irrep) were obtained with Z_1^+ and Z_4^- with $R(F) = 51.6\%$ and 39.6% respectively. However a mixing of the two (Z_1^+ and Z_4^-), with a total of 16 free parameters, leads to excellent agreement factors: $R(F)$ factor and χ^2 are 10% and 10.3 respectively. Figure 3 shows the results of the final refinement, where the experimental structure factors are plotted against the calculated ones. Moreover, as a consistency check, we used the same model with no free parameters to fit the reflections collected in a different position on the sample surface, with excellent agreement. It is therefore important to notice a single Irrep distortion component is not sufficient to explain the full symmetry break of the transformation. A combination of two distortions belonging to different Irreps is indeed necessary. Z_4^- is the main distortion mode associated with the principal magnetic order parameter and has only four active symmetry operations: twofold axis along b, which is compatible with the observation of spontaneous electric polarization in the b direction in this phase and two mirror planes (m_{xy} and m_{yz}), while it doesn't contain inversion symmetry. Z_1^+ is totally symmetric and is a secondary order parameter; in this representation all symmetry

TABLE I. Action of the symmetry operations of the paramagnetic group on the distortion modes associated to different irreducible representations. Symmetry operations are shown in the Seitz notation [31]. The Irreps symmetries are given in Miller and Love notation [32].

	Symmetry Operations							
Irreps	$\{1\|000\}$	$\{2_{00z}\|000\}$	$\{2_{0y0}\|\frac{1}{2}\frac{1}{2}0\}$	$\{2_{x00}\|\frac{1}{2}\frac{1}{2}0\}$	$\{\bar{1}\|000\}$	$\{m_{xy0}\|000\}$	$\{m_{x0z}\|\frac{1}{2}\frac{1}{2}0\}$	$\{m_{0yz}\|\frac{1}{2}\frac{1}{2}0\}$
Z_1^+	1	1	1	1	1	1	1	1
Z_1^-	1	1	1	1	−1	−1	−1	−1
Z_2^+	1	1	−1	−1	1	1	−1	−1
Z_2^-	1	1	−1	−1	−1	−1	1	1
Z_4^+	1	−1	1	−1	1	−1	1	−1
Z_4^-	1	−1	1	−1	−1	1	−1	1
Z_3^+	1	−1	−1	1	1	−1	−1	1
Z_3^-	1	−1	−1	1	−1	1	1	−1

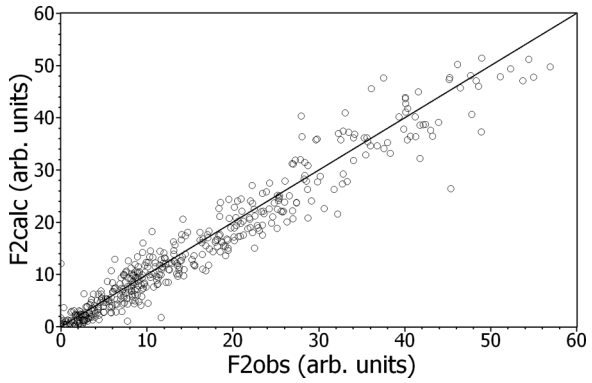

FIG. 3. Results of the refinement with $\mathbf{k}_c = (0\,0\,0.5)$ for the ionic displacement for $HoMn_2O_5$ compound. The experimental structure factors are plotted against the calculated ones. The agreement factors are $R(F)$ factors and χ^2 are 10% and 10.3 respectively.

operations of the high symmetry space group are allowed. Although Z_1^+ is not related to the polar distortions, which are expected to occur at the Γ point (not reported in this manuscript due to the presence of charge peaks and multiple scattering that make the measurement very hard to perform), Z_4^- and Z_1^+ together break inversion and the remaining symmetry is consistent with the point group symmetry $m2m$, in agreement with the previously suggested point group symmetry for the low temperature CM/ferroelectric (FE) phase, magnetic point symmetry $m2'm$ [24,33].

Figure 4 shows the in-plane (ab) ionic displacements pattern (Table II), where the arrows (magnified by 1000 to be visible) represent the ionic displacements. The Ho ions displace in the ab plane. This configuration is very stable and even a refinement with no restraint on these sites leads to the same configuration reported here (error bars $\sim 10^{-4}$). The Ho displacement belongs to the Z_4^- representation. O^{2-} (labeled O2 in Table II) lie in the same mirror plane as Ho ions and share the same in plane displacement as Ho (Wyckoff label $4g$), however because of the large difference in the x-ray

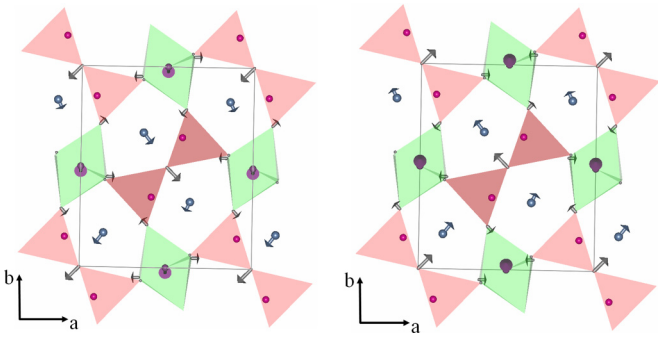

FIG. 4. (Color online) Representation of the observed ionic displacements [$\mathbf{k}_c = (0\,0\,0.5)$] in $HoMn_2O_5$ with arrows (magnified by 1000). The structure is shown in one unit-cell, marked by thin black lines, along the a and b axis. The projection is separately shown for ionic displacements sites belonging to adjacent crystallographic cells along the c direction. The purple (small and light gray), gray, and blue (black) arrows represent ionic displacements on Mn, O^{2+}, and Ho^{3+} sites respectively. Corresponding Mn-O polyhedra are also shown.

atomic form factors between these two species, only the a component shows error bars smaller than the displacement itself. The same is true for the Mn^{3+} ions and O^{2-} (labeled respectively Mn2 and O3 in Table II), lying in the mirror plane at $z = 0.5$ (Wyckoff site $4h$). In this case the error bars are of the same order of magnitude of the displacements and therefore we conclude no displacement on these sites can be measured from the available data. A fit leaving the oxygens sites, labeled O4 (general Wyckoff site $8i$), to move freely lead to good agreement factors, but constraining them with regard to symmetry and in the basal plane, lead to a considerably better fit and smaller error bars. The Mn^{4+} ions (Mn1) sitting in the octahedral sites, displace mainly in the z direction, with a smaller in-plane component, whereas the O1 sites show very large in-plane components, roughly orthogonal to the Mn^{3+}-O-Mn^{3+} chains. The ionic displacements observed are of the order of 10^{-3} Å with error bars in the Ho sites of 10^{-4} Å.

The out of plane component observed on the Mn^{4+} sites is shown in Fig. 5, where the effect of the $\mathbf{k}_c$ propagation vector is shown by the alternating $++--$ periodicity along c. Despite the large number of reflections measured, due to the small

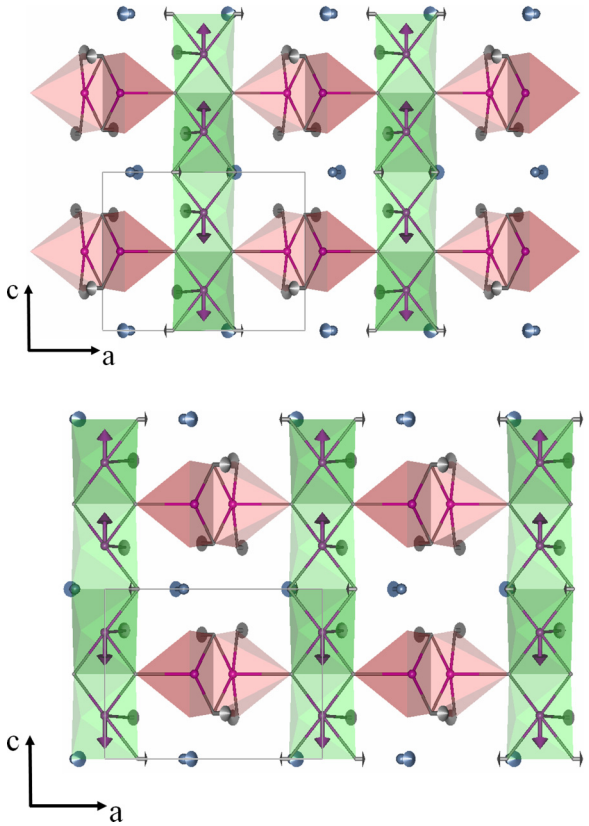

FIG. 5. (Color online) Representation of the observed ionic displacements [$\mathbf{k}_c = (0\,0\,0.5)$] in $HoMn_2O_5$ with arrows (magnified by 1000). The structure is shown in four unit cells, marked by thin black lines (only one cell), along the a and c axis. The projection is separately shown for ionic sites belonging to the first zigzag chain (top) and the second chain (bottom). The purple (small and light gray), gray, and blue (black) arrows represent ionic displacements on Mn, O^{2+} and Ho^{3+} sites respectively. The green (light gray) horizontal arrows inside the Mn^{4+} polyhedra represent the spin ordering of Mn^{4+} from reference [12]. Corresponding Mn-O polyhedra are also shown.

TABLE II. Fourier coefficients (in Å) obtained from least-square refinements of the single crystal SL peaks for $HoMn_2O_5$ at $T = 22$ K (See text for details). The Fourier coefficients for each site in the primitive unit-cell are given along crystallographic direction (x,y,z) and labeled D. Error bars are given for all parameters within parenthesis.

Label	Atom	Position	D_x	D_y	D_z
HO-1	Ho^{3+}	(0.1371 0.1709 0)	–0.00037(1)	–0.00047(1)	0
HO-3	Ho^{3+}	(0.3629 0.6709 0)	0.00037(1)	–0.00047(1)	0
HO-4	Ho^{3+}	(0.6371 0.3291 0)	–0.00019(1)	–0.00040(1)	0
HO-2	Ho^{3+}	(0.8629 0.8291 0)	0.00019(1)	–0.00040(1)	0
Mn1-1	Mn^{4+}	(0.5 0 0.2551)	0	–0.00029(2)	–0.00112(4)
Mn1-2	Mn^{4+}	(0 0.5 0.7449)	0	0.00029(2)	–0.00112(4)
Mn1-3	Mn^{4+}	(0.5 0 0.7449)	0	0.00029(2)	–0.00112(4)
Mn1-4	Mn^{4+}	(0 0.5 0.2551)	0	–0.00029(2)	–0.00112(4)
Mn2-1	Mn^{3+}	(0.4119 0.3508 0.5)	0	0	0
Mn2-2	Mn^{3+}	(0.5881 0.6492 0.5)	0	0	0
Mn2-3	Mn^{3+}	(0.0881 0.8508 0.5)	0	0	0
Mn2-4	Mn^{3+}	(0.9119 0.1492 0.5)	0	0	0
O1-1	O^{2-}	(0 0 0.2680)	–0.00056(7)	–0.0006(1)	0
O1-2	O^{2-}	(0.5 0.5 0.7320)	–0.00056(7)	0.0006(1)	0
O1-3	O^{2-}	(0 0 0.7320)	0.00056(7)	0.0006(1)	0
O1-4	O^{2-}	(0.5 0.5 0.2680)	0.00056(7)	–0.0006(1)	0
O2-1	O^{2-}	(0.1533 0.4499 0)	0.00032(8)	0	0
O2-2	O^{2-}	(0.8467 0.5501 0)	–0.00032(8)	0	0
O2-3	O^{2-}	(0.3467 0.9499 0)	–0.00032(8)	0	0
O2-4	O^{2-}	(0.6533 0.0501 0)	0.00032(8)	0	0
O3-1	O^{2-}	(0.1420 0.4344 0.5)	0	0	0
O3-2	O^{2-}	(0.8580 0.5656 0.5)	0	0	0
O3-3	O^{2-}	(0.3580 0.9344 0.5)	0	0	0
O3-4	O^{2-}	(0.6420 0.0656 0.5)	0	0	0
O4-1	O^{2-}	(0.3897 0.2118 0.2435)	–0.00022(5)	0.00024(8)	0
O4-2	O^{2-}	(0.6103 0.7882 0.2435)	–0.00022(5)	–0.00024(8)	0
O4-3	O^{2-}	(0.1103 0.7118 0.7565)	–0.00022(5)	–0.00024(8)	0
O4-4	O^{2-}	(0.8897 0.2882 0.7565)	–0.00022(5)	0.00024(8)	0
O4-5	O^{2-}	(0.6103 0.7882 0.7565)	0.00022(5)	0.00024(8)	0
O4-6	O^{2-}	(0.3897 0.2118 0.7565)	0.00022(5)	–0.00024(8)	0
O4-7	O^{2-}	(0.8897 0.2882 0.2435)	0.00022(5)	–0.00024(8)	0
O4-8	O^{2-}	(0.1103 0.7118 0.2435)	0.00022(5)	0.00024(8)	0

sensitivity of the x-ray to light elements, ionic displacements of the oxygens sites show large error bars ($\gtrsim$30%). However, these displacements are essential to the model stability.

IV. MODEL FOR THE PROPAGATION ALONG THE *C* AXIS

In contrast with the complexity of the ionic displacement pattern in the *ab* plane, the out of plane Mn^{4+} displacement follows a simple ordering. This periodicity could be used, together with the magnetic ordering information, to determine the stabilization conditions for the magnetic propagation vector $k_z = 1/4$ and to find the relative phases of the magnetic and crystal structures, effectively linking the magnetic and the crystallographic structure by removing the inherent phase ambiguity arisen from structural refinements alone. Here we use an approach based on the linear-chain model, in which only the *c* and *a* components, respectively of displacements (δ) and magnetic nearest-neighbor (NN, J_1, J_2, where J_1 is the Mn^{4+}-Mn^{4+} intracell exchange constant, J_2 is the intercell Mn^{4+}-Mn^{4+} exchange) and next-nearest-neighbor (NNN, J_3) interactions are considered (Fig. 6) [34]. The Mn^{4+} in-plane spins are defined as:

$$\begin{aligned} s_1 &= S\cos(2\pi q_z R_L + \phi) \\ s_2 &= S\cos(2\pi q_z R_L + \phi), \end{aligned} \tag{2}$$

where R_L is the unit cell index, q_z is the magnetic propagation vector component (along z) and ϕ is the phase between the structure and the magnetic sublattice. ϕ being expressed in radians, so it relates to the tabulated values as $\phi = 2\pi\Phi$ (Φ are site-dependent relative phases [12]). We can construct an idealized one-dimensional model, coupled through nearest-neighbor interactions (J_1 and J_2) and next-nearest-neighbor interactions (J_3).

$$\begin{aligned} J_1 &= J_1 \\ J_{2a} &= J_2(1-\delta) \\ J_{2b} &= J_2(1+\delta) \\ J_{3a} &= J_3(1-\delta) \\ J_{3b} &= J_3(1+\delta), \end{aligned} \tag{3}$$

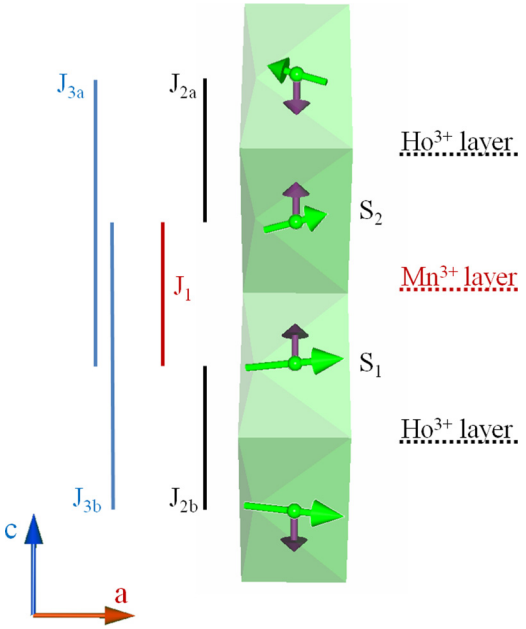

FIG. 6. (Color online) Labeling scheme and relevant interactions for the linear-chain model. Purple (dark gray) arrows represent ionic displacements while green (light gray) arrows represent the spin ordering from Ref. [12].

where the J_2 and J_3 exchange constants are split as function of the ionic displacement δ. The total energy per unit cell is:

$$E = \frac{1}{N}\sum_{R_L} J_1 s_1 \cdot s_2 + \frac{1}{2}(J_{2a} s_2 \cdot s_1' + J_{2b} s_1 \cdot s_2') + \frac{1}{2}(J_{3a} s_1 \cdot s_1' + J_{3b} s_2 \cdot s_2'), \quad (4)$$

where the primed spins belong to the neighboring unit cells. By replacing the expressions of the spins and the exchange integrals in Eq. (4) and minimizing the energy with respect to ϕ, we obtain the relative phases between the magnetic sublattice and the crystal structure: the coupling of the ionic displacements with J_2 and J_3 leads to the stabilization of the magnetic structure at a phase $\phi = \pi/4$ with respect to the crystal structure ($\Phi = 1/8$). This phase allows for even moment magnitudes throughout the system, in contrast for example to a phase of $\Phi = 1/4$, which leads to an alternating stack along c of $[+0-0]$ magnetic moments.

V. CONCLUSIONS

In this work we develop a method to measure and refine tiny collective ionic displacements in a complex magnetic system. Although the crystal studied is a multiferroic compound, this method is not restricted to this class of materials. In fact no external perturbation (electric/magnetic field) was applied therefore no magnetoelectric domain has been selected. We have demonstrated that very high precisions in the determination of the magnetostriction induced ionic displacement pattern (∼100 fm, light atoms) are achievable. Moreover this work shows the first direct evidence of a subtle symmetry-breaking transition in the CM magnetic phase of $HoMn_2O_5$. Finally, we have also shown that by knowing both the magnetic structure and the magnetically induced strain waves, it is possible to determine the global phase between them removing any phase ambiguity in the magnetic structure determination. These high-accuracy measurements could be used to both validate and challenge *ab initio* theoretical predictions of displacement modes due to competing (super)exchange interactions in (f electrons) frustrated magnetic materials.

ACKNOWLEDGMENT

Work at Rutgers was supported by the NSF Grant No. DMR-1104484.

[1] M. B. Walker, Phys. Rev. B **22**, 1338 (1980).
[2] J. P. Hill, G. Helgesen, and D. Gibbs, Phys. Rev. B **51**, 10336 (1995).
[3] Y. Tsunoda, M. Mori, N. Kunitomi, Y. Teraoka, and J. Kanamori, Solid State Commun. **14**, 287 (1974).
[4] C. Eagen and S. Werner, Solid State Commun. **16**, 1113 (1975).
[5] A. de Oliveira, P. de Souza, C. Giles, I. Mazzaro, and P. de Camargo, J. Magn. Magn. Mater. **310**, e316 (2007).
[6] J. Strempfer, B. Bohnenbuck, M. Mostovoy, N. Aliouane, D. N. Argyriou, F. Schrettle, J. Hemberger, A. Krimmel, and M. v. Zimmermann, Phys. Rev. B **75**, 212402 (2007).
[7] A. Stunault, J. Schweizer, F. Givord, C. Vettier, C. Detlefs, J.-X. Boucherle, and P. Lejay, J. Phys.: Condens. Matter **21**, 376004 (2009).
[8] T. Asaka, X. Z. Yu, Y. Hiraoka, K. Kimoto, T. Hirayama, T. Kimura, and Y. Matsui, Phys. Rev. B **83**, 130401 (2011).
[9] N. Hur, S. Park, P. A. Sharma, J. S. Ahn, S. Guha, and S.-W. Cheong, Nature (London) **429**, 392 (2004).
[10] L. C. Chapon, P. G. Radaelli, G. R. Blake, S. Park, and S.-W. Cheong, Phys. Rev. Lett. **96**, 097601 (2006).
[11] N. Lee, C. Vecchini, Y. J. Choi, L. C. Chapon, A. Bombardi, P. G. Radaelli, and S.-W. Cheong, Phys. Rev. Lett. **110**, 137203 (2013).
[12] C. Vecchini, L. C. Chapon, P. J. Brown, T. Chatterji, S. Park, S.-W. Cheong, and P. G. Radaelli, Phys. Rev. B **77**, 134434 (2008).
[13] C. Wang, G.-C. Guo, and L. He, Phys. Rev. Lett. **99**, 177202 (2007).
[14] H. C. Walker, F. Fabrizi, L. Paolasini, F. de Bergevin, J. Herrero-Martin, A. T. Boothroyd, D. Prabhakaran, and D. F. McMorrow, Science **333**, 1273 (2011).
[15] N. Aliouane, D. N. Argyriou, J. Strempfer, I. Zegkinoglou, S. Landsgesell, and M. v. Zimmermann, Phys. Rev. B **73**, 020102 (2006).
[16] S. W. Lovesey and S. P. Collins, *X-Ray Scattering and Absorption by Magnetic Materials* (Clarendon, Oxford, 1996).
[17] W. Sławiński, R. Przeniosło, I. Sosnowska, M. Bieringer, I. Margiolaki, and E. Suard, Acta Crystallogr. Sect. B **65**, 535 (2009).

[18] G. Beutier, A. Bombardi, C. Vecchini, P. G. Radaelli, S. Park, S.-W. Cheong, and L. C. Chapon, Phys. Rev. B **77**, 172408 (2008).
[19] L. M. Volkova and D. V. Marinin, J. Phys.: Condens. Matter **21**, 015903 (2009).
[20] I. Radulov, V. Lovchinov, D. Dimitrov, and A. Apostolov, J. Phys. Conf. **153**, 012064 (2009).
[21] http://www.diamond.ac.uk/Home/Beamlines/I16.html.
[22] S. P. Collins, A. Bombardi, A. R. Marshall, J. H. Williams, G. Barlow, A. G. Day, M. R. Pearson, R. J. Woolliscroft, R. D. Walton, G. Beutier, and G. Nisbet, AIP Conf. Proc. **1234**, 303 (2010).
[23] J. Rodriguez-Carvajal, Physica B **192**, 55 (1993).
[24] G. R. Blake, L. C. Chapon, P. G. Radaelli, S. Park, N. Hur, S.-W. Cheong, and J. Rodríguez-Carvajal, Phys. Rev. B **71**, 214402 (2005).
[25] J. Koo, C. Song, S. Ji, J.-S. Lee, J. Park, T.-H. Jang, C.-H. Yang, J.-H. Park, Y. H. Jeong, K.-B. Lee, T. Y. Koo, Y. J. Park, J.-Y. Kim, D. Wermeille, A. I. Goldman, G. Srajer, S. Park, and S.-W. Cheong, Phys. Rev. Lett. **99**, 197601 (2007).
[26] H. T. Stokes, D. M. Hatch, and B. J. Campbell, ISOTROPY, stokes.byu.edu/isotropy.html (2007).
[27] D. Orobengoa, C. Capillas, M. I. Aroyo, and J. M. Perez-Mato, J. Appl. Crystallogr. **42**, 820 (2009).
[28] M. I. Aroyo, J. M. Perez-Mato, D. Orobengoa, E. Tasci, G. de la Flor, and A. Kirov, Bulg. Chem. Commun. **43**(2) 183 (2011).
[29] M. I. Aroyo, J. M. Perez-Mato, C. Capillas, E. Kroumova, S. Ivantchev, G. Madariaga, A. Kirov, and H. Wondratschek, Z. Kristallogr. **221**, 15 (2006).
[30] M. I. Aroyo, A. Kirov, C. Capillas, J. M. Perez-Mato, and H. Wondratschek, Acta Crystallogr. A **62**, 115 (2006).
[31] D. B. Litvin and V. Kopský, Acta Crystallogr. Sect. A **67**, 415 (2011).
[32] S. C. Miller and W. F. Love, *Tables of Irreducible Representations of Space Groups and Co-Representations of Magnetic Space Groups* (Boulder, Colorado, 1967).
[33] P. G. Radaelli and L. C. Chapon, Phys. Rev. B **76**, 054428 (2007).
[34] P. G. Radaelli and L. C. Chapon, J. Phys.: Condens. Matter **20**, 434213 (2008).